Microstructure and mechanical properties of Haynes 282 superalloy produced by laser powder bed fusion

Materials Today Communications 26 (2021) 102038

Contents lists available at ScienceDirect

Materials Today Communications

journal homepage: www.elsevier.com/locate/mtcomm

Microstructure and mechanical properties of Haynes 282 superalloy produced by laser powder bed fusion

Abdul Shaafi Shaikh [a,b,*], Fiona Schulz [a], Kevin Minet-Lallemand [b], Eduard Hryha [a]

[a] Chalmers University of Technology, Department of Industrial and Material Science, Rännvägen 2A, Campus Johanneberg, 41296, Gothenburg, Sweden
[b] Electro Optical Systems Finland Oy, Lemminkäisenkatu 36, 20520, Turku, Finland

ARTICLE INFO

Keywords:
Nickel-base superalloy
High temperature material
Haynes 282
Additive manufacturing
Laser powder bed fusion
Microstructure
Mechanical performance

ABSTRACT

Ni-base superalloys are essential materials for high-temperature applications in the energy and aerospace sectors. Significant benefits in design, function, and manufacture of high-temperature components may be realized from additive manufacturing (AM) of these materials. However, because of cracking issues during AM fabrication, only a handful of materials have been tried and qualified. This article provides an initial evaluation of the processability and properties of Haynes 282 by laser-powder bed fusion (LPBF), which is a relatively new Ni-base superalloy with properties superior to those of many legacy wrought superalloys. The results demonstrated that crack-free Haynes 282 can be manufactured by means of LPBF with full density. The mechanical properties at ambient temperature exceeded the properties of the reference material in the as-built and heat-treated conditions, albeit with significant anisotropy. Mechanical properties at 800 °C indicated that the yield strength of heat-treated Haynes 282 by LPBF was comparable to that of the reference material, however, ductility was significantly reduced. Promising stress rupture performance also indicates that Haynes 282 is an ideal candidate for adoption in additive manufacturing, especially if heat treatments can be re-designed for the additively manufactured as-built microstructure.

1. Introduction

Nickel-base superalloys are a unique class of engineering materials due to their exceptional combination of high strength at elevated temperature, resistance to corrosion and oxidation, and good creep and fatigue performance. However, because of these properties, many Ni-base superalloys have proven difficult to fabricate into components with complex geometries. Additive manufacturing (AM), in particular laser powder bed fusion (LPBF), has seen increasing industrial adoption for prototyping and mass production of metal components. LPBF is a layer-by-layer process, by which a shape is scanned and melted using a high powered laser into a layer of metal powder until the desired 3D part is formed. It can produce parts with densities and material properties that equal or exceed those of conventionally manufactured materials [1]. LPBF also allows the consolidation of complex assemblies and the manufacture of internal features such as cooling channels, and it reduces design iterations and manufacturing lead time. Given these advantages, it has been applied to the manufacture of complex parts such as gas turbine components [2,3]. The number of high-temperature materials available for LPBF processing has, however, remained limited, creating a need to adopt new materials into the range of LPBF processes.

Ni-base superalloys have received much attention in AM research publications, but the selection of alloys available for LPBF is still severely limited. Most published work has focused on solid solution strengthened alloys such as IN625 and Hastelloy-X, or the γ'' strengthened IN718. Research on γ' strengthened alloys such as IN738LC and CM247LC has highlighted significant challenges in manufacturing related to cracking during and after the LPBF process [2,4–8]. However, there is as yet little available research on LPBF of Haynes 282 [9–11]. As Haynes 282 is known to possess excellent fabricability, there is considerable incentive to evaluate the processability and performance of the alloy in LPBF-manufactured form.

Haynes 282 is a Ni-base superalloy that was conceived as a breakthrough material. In early publications by Pike, it was presented as a novel wrought Ni-base superalloy with a balance of mechanical properties and fabricability superior to those of other common wrought alloys such as Waspaloy [12,13]. Initially produced and adopted for structural applications in industrial gas turbines and aero-engines,

* Corresponding author at: Chalmers University of Technology, Department of Industrial and Material Science, Rännvägen 2A, Campus Johanneberg, 41296, Gothenburg, Sweden.
E-mail address: abdulsh@chalmers.se (A.S. Shaikh).

https://doi.org/10.1016/j.mtcomm.2021.102038
Received 5 November 2020; Received in revised form 7 January 2021; Accepted 10 January 2021
Available online 14 January 2021

Haynes 282 has more recently also been considered for use in construction of equipment for Advanced-Ultrasupercritical power plants, chiefly due to its formability, repairability, and creep strength [14]. Haynes 282 achieves its properties through a relatively low volume fraction of γ' strengthening precipitates (to which its good weldability is also attributed [13]) and through solid solution strengthening by a generous addition of Mo. The microstructure also includes MC, M_6C, and $M_{23}C_6$ carbides, as well as M_5B_3 borides, all of which are understood to play a role in the strengthening of the alloy at different temperatures. Creep performance at temperatures up to 927 °C was shown to be competitive with that of other wrought alloys [12]. It is also worth noting that the application temperatures of Haynes 282 extend well above the ~ 650 °C limit of the widely used Inconel 718 [15].

While the cooling rates for the LPBF process are known to be closer to rapid solidification processes than to conventional welding, alloys with complex compositions are nevertheless prone to cracking [5,7,16,17]. Therefore, the weldability of a material is often taken as an indicator of whether it will be suitable for fusion processes such as LPBF. Generally, superalloys are susceptible to various forms of cracking when welded and thus require extensive process development in LPBF. Hot cracking (solidification and liquation cracking) of Haynes 282 has been studied by several authors. Susceptibility of wrought Haynes 282 to solidification cracking was found to be considerably lower than that of other wrought alloys, including IN718 [18–21]. Susceptibility to heat affected zone (HAZ) liquation cracking was also observed to be lower than in comparable alloys, and detected cracks were suspected to be caused by liquation of Cr-rich carbides [18]. Finally, the strain age cracking susceptibility of Haynes 282 has also been examined and found to be rather low due to the slow precipitation of γ' that is characteristic of the alloy [22].

Being a precipitation strengthened alloy, Haynes 282 requires heat treatment to realize its advantageous microstructure and properties. The heat treatment recommended by Haynes International Inc. consists of a solution treatment above the γ' and carbide solvus temperatures, followed by a 2-step ageing process at 1010 °C and 788 °C to precipitate grain boundary carbides and fine γ' particles, respectively [14,23]. Alternative heat treatments have been proposed by several researchers: both Joseph et al. and Polkowska et al. proposed lower ageing temperatures [23,24], and Unocic et al. proposed a single-step ageing at 800 °C [25].

The mechanical properties of Haynes 282 across a range of temperatures and product forms are well documented by a number of authors. Official documentation from Haynes International Inc. shows that the age hardened sheet material exhibits yield stresses around 700 MPa, ultimate tensile stresses around 1140 MPa, and elongation values of 30% [26]. Similar findings have also been reported by other authors [23,27]. At temperatures up to 700 °C very little change in yield strength is observed, while at 816 °C the yield strength drops to around 575 MPa with 28% elongation [26].

There are few published reports on AM of Haynes 282. Work by Unocic et al. has shown that electron beam melting (EBM) can feasibly produce Haynes 282 parts with low defect counts. After EBM the microstructure was seen to be pre-aged and to have a highly columnar grain structure [28]. Directed energy deposition (DED) of Haynes 282, as studied by Ramakrishnan and Dinda, can be used to deposit the alloy with sound density, albeit with a cored microstructure having significant heterogeneity between dendrite core and interdendritic regions [29]. The potential of LPBF process development for successful fabrication of Haynes 282 was recently shown by Otto et al. [9], and post-processing routes explored by Deshpande et al. and Christofidou et al. indicated that favourable microstructure and properties are achievable in several heat treatment conditions [10,11]. Consequently, this article provides further evaluation of the LPBF processability of Haynes 282, and assesses the resulting microstructure and mechanical properties.

2. Materials and methods

Haynes 282 powder with a standard chemical composition (see Table 1) provided by Höganäs AB was used in this study. The powder was manufactured by vacuum inert gas atomization, and hence was characterised by a spherical morphology. The powder had a particle size distribution between 15 μm and 45 μm. An EOS M290 LPBF system having a 400 W Yb-fibre laser and a build envelope of 250 mm x 250 mm x 325 mm was used for LPBF processing. The machine was operated with a 40 μm layer thickness, and samples were built using process parameters developed by EOS (providing the basis for a process parameter set to be released by the hardware manufacturer in the near future). Development of process parameters was performed in the volumetric energy density (E_v) range between 30 J/mm^3 and 75 J/mm^3, and optimal process parameters having a E_v of 59 J/mm^3 were selected for sample manufacturing. The LPBF process was performed under an Ar gas atmosphere, and samples were built onto a steel build platform which was kept at 40 °C throughout the building process. Manufactured samples included cuboids having sides of 15 mm x 15 mm and a height of 18 mm. Cylindrical tensile test blanks (80 mm x 11 mm diameter) and blanks for stress rupture testing (100 mm x 10 mm diameter) were built in horizontal and vertical orientations.

The produced samples were removed from the steel build plate using a bandsaw. Selected samples were heat treated according to the standard 3-step heat treatment recommended by Haynes International. The heat treatment (steps given in Table 2) was performed in a TAV H4-S type industrial vacuum furnace (TAV Vacuum Furnaces SPA, Caravaggio BG, Italy) in which pressurized Ar gas was used for cooling.

Samples in the as-built or heat-treated condition were sectioned and mounted in Struers PolyFast conductive resin. Metallographic preparation consisted of progressive grinding using silicon carbide papers up to P1000, followed by a 3 μm and 1 μm polish with diamond paste. Samples for microstructure analysis were electrolytically etched using 10% oxalic acid at 6 V for up to 5 seconds. Optical microscopy was performed using an Olympus GX51 microscope with a motorized stage. A Zeiss GeminiSEM-450 scanning electron microscope (SEM) with field emission gun source was used for microanalysis. This microscope was fitted with a Bruker Quantax FlatQuad Energy Dispersive X-Ray Spectroscopy (EDX) detector which enables elemental mapping of microstructure at sub-micron resolutions. Grain size analysis was performed using area measurement, and precipitate size analysis was performed on SEM micrographs using the ImageJ software.

Samples for room-temperature and elevated-temperature tensile testing were machined to a gauge length of 25.4 mm and gauge diameter of 4.7 mm. Tensile testing at room temperature was performed according to ISO 6892-1, with a strain rate of 0.00025 s^{-1} until yield followed by 0.002 s^{-1} until fracture. Elevated-temperature tensile testing at 800 °C was performed in accordance with ISO 6892-2, with a strain rate of 0.00025 s^{-1} until yield followed by 0.0014 s^{-1} until fracture. Yield strength, ultimate tensile strength, and percentage elongation were determined according to ISO 6892 ($R_{P0.2}$, R_m, and A%, respectively). Constant-load tensile stress rupture testing was performed according to ASTM E139 using machined samples with a 6 mm diameter at the gauge length. All reported tensile test and stress rupture results are averages of three samples per test condition. Fractography analysis was performed using a Zeiss Leo 1550 Gemini FEG-SEM.

3. Results

Near-full density was achieved in the samples produced by the applied LPBF process, as can be seen from Fig. 1. No large pores, inclusions, or lack-of-fusion defects were observed in the cross-section. Image analysis showed that the total fraction of defects was only 0.015%, which is equivalent to 99.985% dense material. Detailed examination revealed occasional small pores with diameters between 10 μm and 30 μm which appeared at random and are known to be a

Table 1
Composition of Haynes 282 powder in wt.%.

Cr	Co	C	Mo	Ti	Al	B	Ni	O	N	S	P	Si	Mn
19.1	10.2	0.050	8.5	2.1	1.6	0.003	Bal	0.011	0.007	< 0.005	0.001	0.020	< 0.1

Table 2
Heat treatment applied to Haynes 282 laser powder bed fusion (LPBF) samples.

Step	Temperature (°C)	Holding time (hrs)	Cooling
1	1150	2 h	Cooling with forced Ar gas, ~20 °C/min
2	1010	2 h	Cooling with forced Ar gas, ~20 °C/min
3	788	8 h	Cooling with forced Ar gas, ~20 °C/min

common discontinuity in LPBF materials. Limited trials conducted during initial process parameter screening showed that lack-of-fusion defects increased below E_v of 45 J/mm^3, but no cracks were observed up to highest used E_v of 75 J/mm^3. The etched micrograph in Fig. 1(b) shows that grains in the as-built material are narrow and columnar, and are aligned with the direction of build-up, denoted by "Z".

Fig. 2 shows that the solid material consists of individual melt tracks stacked in layers, overlapping each other laterally while also achieving full fusion between layers. Etching has highlighted the melt track boundaries as well as grain boundaries, which can be seen as dark lines across the melt tracks. The differing dimensions and appearances of the melt tracks in Fig. 2(a) are a result of rotation of the scanning direction from one layer to the next, an effect which can be seen more clearly in Fig. 2(b).

A closer look at the as-built microstructure in SEM micrographs shows a fine dendritic solidification structure, as presented in Fig. 3. Packets of dendrites with similar growth orientations can be observed in Fig. 3(a), and Fig. 3(b) shows three different grains in which all

Fig. 1. Cross-section of as-built LPBF Haynes 282 (a) plain-polished and (b) etched. "Z" indicates direction of layer-wise build-up.

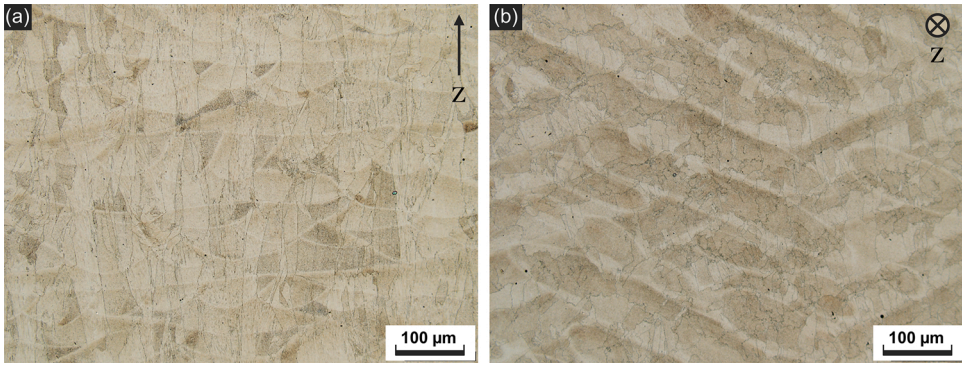

Fig. 2. Optical micrographs of as-built LPBF Haynes 282 (a) cross-section parallel to build direction and (b) cross-section perpendicular to the build direction. Electrolytically etched with 10 % oxalic acid.

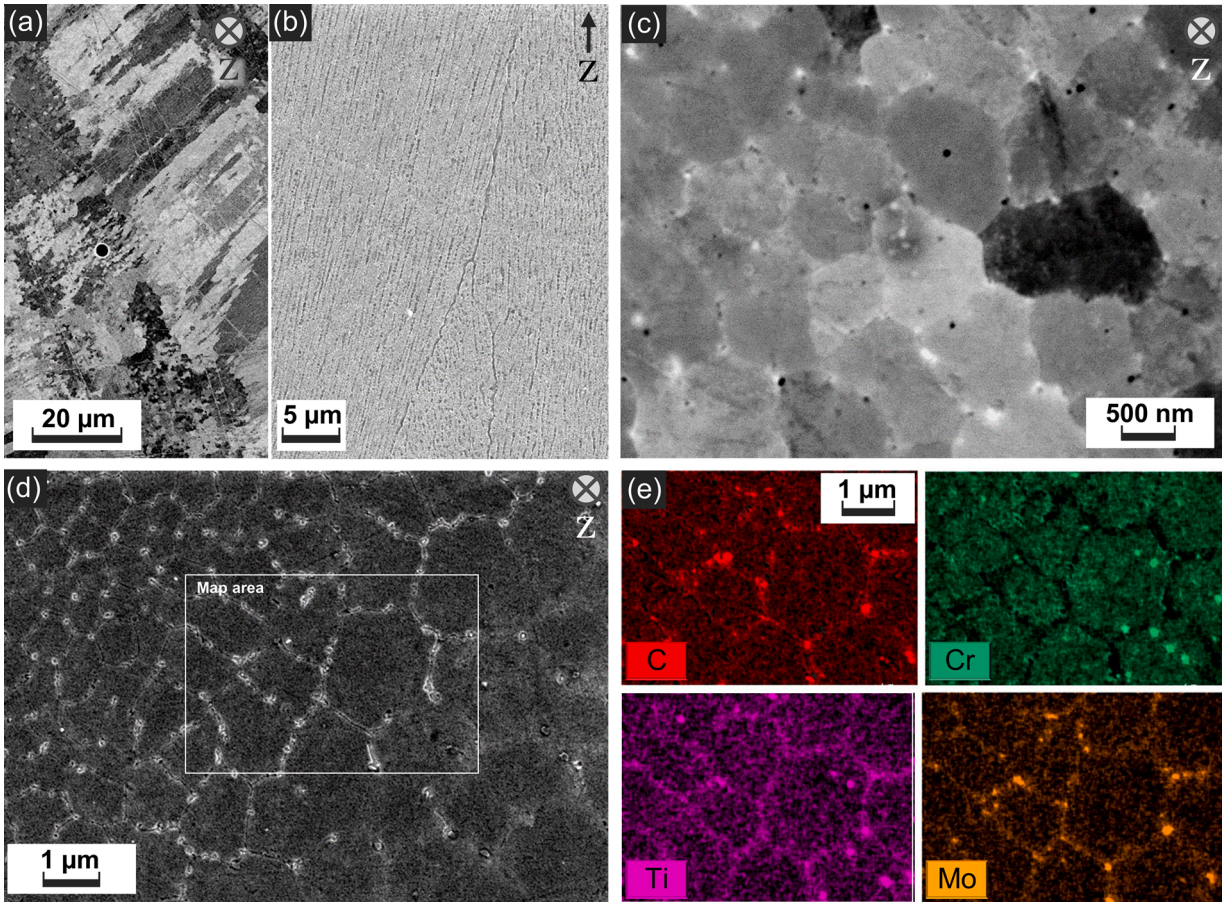

Fig. 3. Microstructure of LPBF Haynes 282 in the as-built condition. (a) and (c) back-scattered electron scanning electron microscope (BSE-SEM) micrographs; (b) and (d) SE-SEM micrographs; (e) Energy Dispersive X-Ray Spectroscopy (EDX) analysis maps.

dendrites are growing approximately along the building direction. Primary dendrite arm spacing was observed to be close to 1 µm, with no clear indication of secondary arms. Fig. 3(c) exhibits a region with dendrites aligned perpendicular to the plane of cross-section. Compositional contrast from the back-scattered electron (BSE) detector shows bright spots between dendrite cores, which suggests segregation of heavy elements to the interdendritic regions. EDX analysis mapping of the cellular-dendritic structure is presented in Fig. 3(d) and (e). Selected elemental maps shown in the figure highlight the segregation of C, Ti, and Mo to the interdendritic regions. The dendrite cores are conversely rich in Cr, Ni, and Co, and Al was found to be evenly distributed throughout the solidification microstructure, as expected. The small dark spots observed at various locations in BSE micrographs are suspected to be oxides, as these appear darker in BSE imaging mode [30–32].

Optical micrographs of the microstructure after full heat treatment are shown in Fig. 4. No recrystallization was observed in the heat-treated samples. The melt track boundaries are no longer visible owing to the homogenization effect of the heat treatment. Grain boundaries appear more distinct due to decoration by carbides (as shown in further results below) and appear as a darker contrast. The grain structure is observed as anisotropic, showing long and narrow grains along the building direction (ZY-plane) and small equiaxed grains perpendicular to the building direction (XY-plane). This is indicative of columnar grains and characteristic of microstructures produced by LPBF [11,30,31,33].

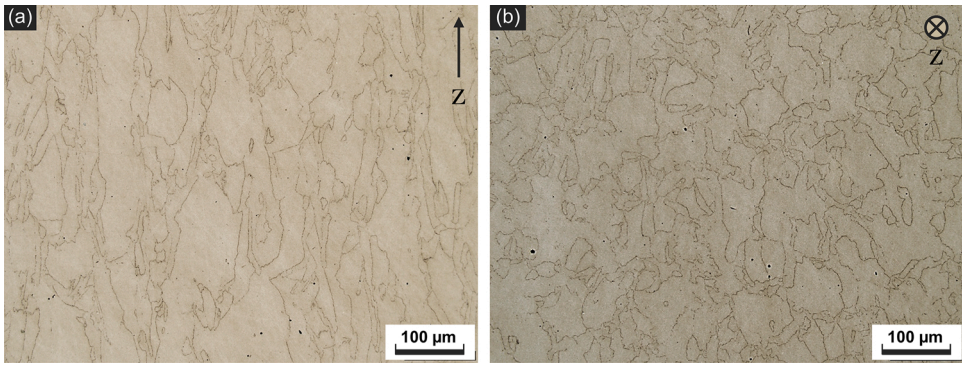

Fig. 4. Optical micrographs showing grain structure of LPBF Haynes 282 after heat treatment. (a) cross-section parallel to build direction and (b) cross-section perpendicular to the build direction. Electrolytically etched with 10 % oxalic acid.

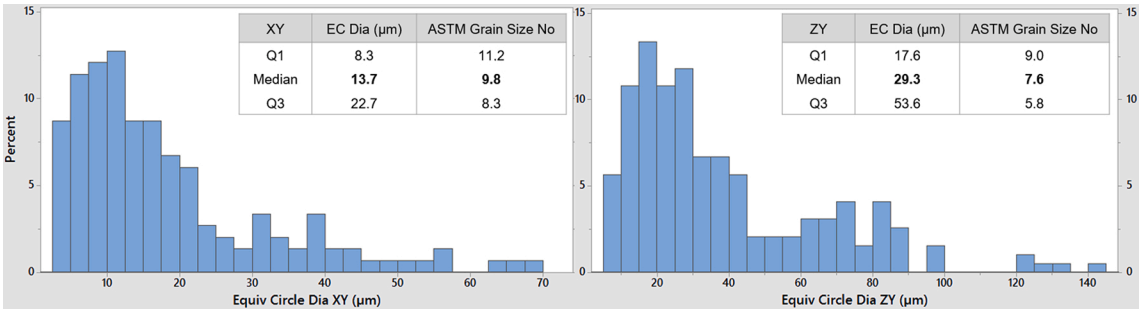

Fig. 5. Distribution of grain sizes in the planes perpendicular (XY) and parallel (ZY) to the build direction in LPBF Haynes 282 after full heat treatment. EC: equivalent circle.

Analysis of grain size (see Fig. 5) shows that the distribution of grains is skewed towards finer grain sizes. As the grains do not appear spherical in shape when viewed in cross-section, the measure of "equivalent circle diameter" has been calculated based on grain area. Fig. 5 shows that the median grain size in the XY-plane is extremely fine, with even the third quartile at only a 22.7 μm equivalent circle diameter, which is equivalent to ASTM grain size number of ~8. In the ZY-plane larger grains can be found, due to their columnar shape, but the median ASTM grain size number is still 7.6, which can be considered fine-grained. However, a small percentage of grains are exceptionally large, with equivalent circle diameters exceeding 120 μm, and these can also be observed in the optical micrograph in Fig. 4(a).

The fully heat-treated microstructure displays carbides along the grain boundaries, as can be observed in the BSE detector micrograph in Fig. 6(a). It can also be seen that the cellular-dendritic solidification microstructure has not been fully homogenized following the applied heat treatment, and sub-grain boundaries are still evident. Fig. 6(b) shows that carbides with blocky morphology are found at the grain boundaries but are not in the continuous "stone wall" arrangement that has been reported for the wrought material. In addition to inter-granular carbides, numerous intra-granular carbides can also be found in the microstructure. At higher magnification, the intra-granular γ + γ' microstructure can clearly be seen, as can the carbides and grain boundary γ', as depicted in Fig. 6(c). Additionally, small γ' precipitates can also be observed at the carbide-matrix interface.

More detailed analysis of the grain boundary region, seen in Fig. 7 (a), shows several different particles with distinct chemical compositions. Based on EDX maps in Fig. 7(b), we can determine that these include Mo-rich carbides, small Cr-rich carbides, and several <100 nm sized Ti-rich carbide particles. Not all the Tirich carbides are clearly visible in the electron micrograph due to the background of γ + γ'. A layer of Al-rich phase is also noticeable at the grain boundaries and at the interface between carbides and the γ matrix. This is assumed to be a layer of γ' formed by reaction of the γ matrix with the carbides, which is discussed in later sections of this article. Similar grain boundary constituents were observed at several locations, with another instance shown in Fig. 7(c) and (d). The grain boundary runs from the bottom left to the top right of the micrograph. Several particles are observed in which carbon is concentrated, including two Cr-rich carbides and at least six small Ti-rich carbides. The Cr-rich carbides also give a weak indication of Mo content. Between the carbides and at the grain boundary a clear concentration of Al and Ni can be observed, further suggesting this phase to be grain boundary γ'.

From other authors' extensive microanalyses of phases in Haynes

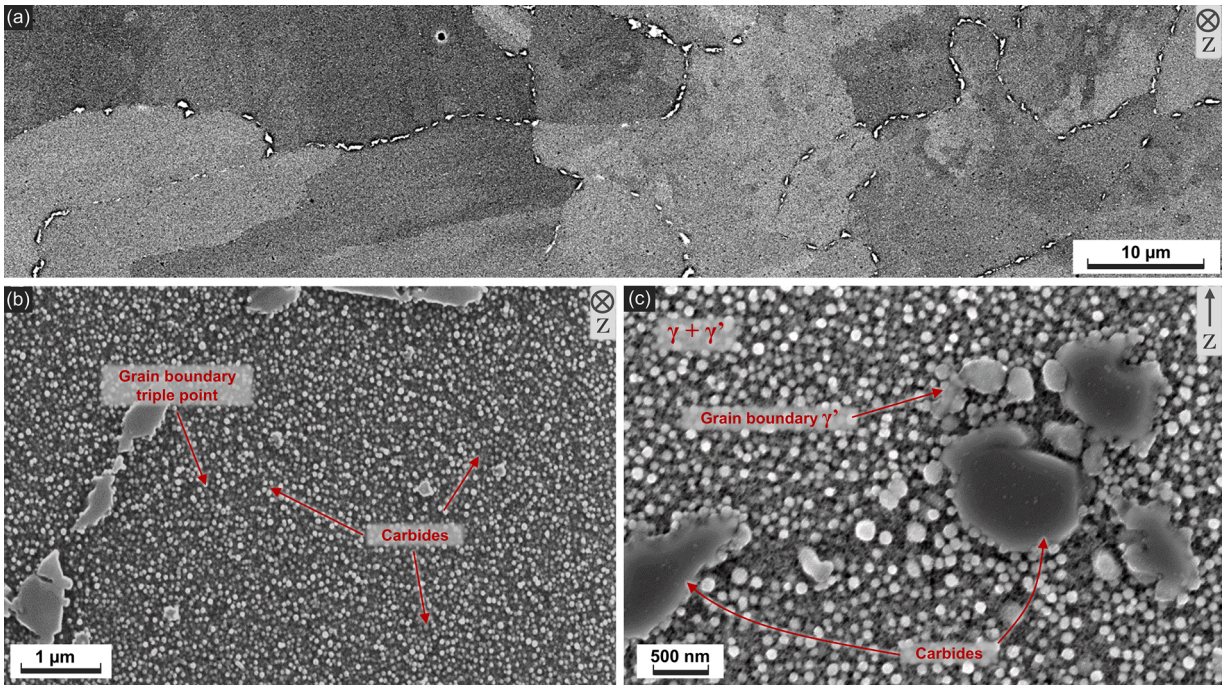

Fig. 6. Microstructure of fully heat-treated LPBF Haynes 282. (a) BSE-SEM micrograph; (b) SE-SEM micrograph showing grain boundary triple point; (c) SE-SEM micrograph showing grain boundary phases.

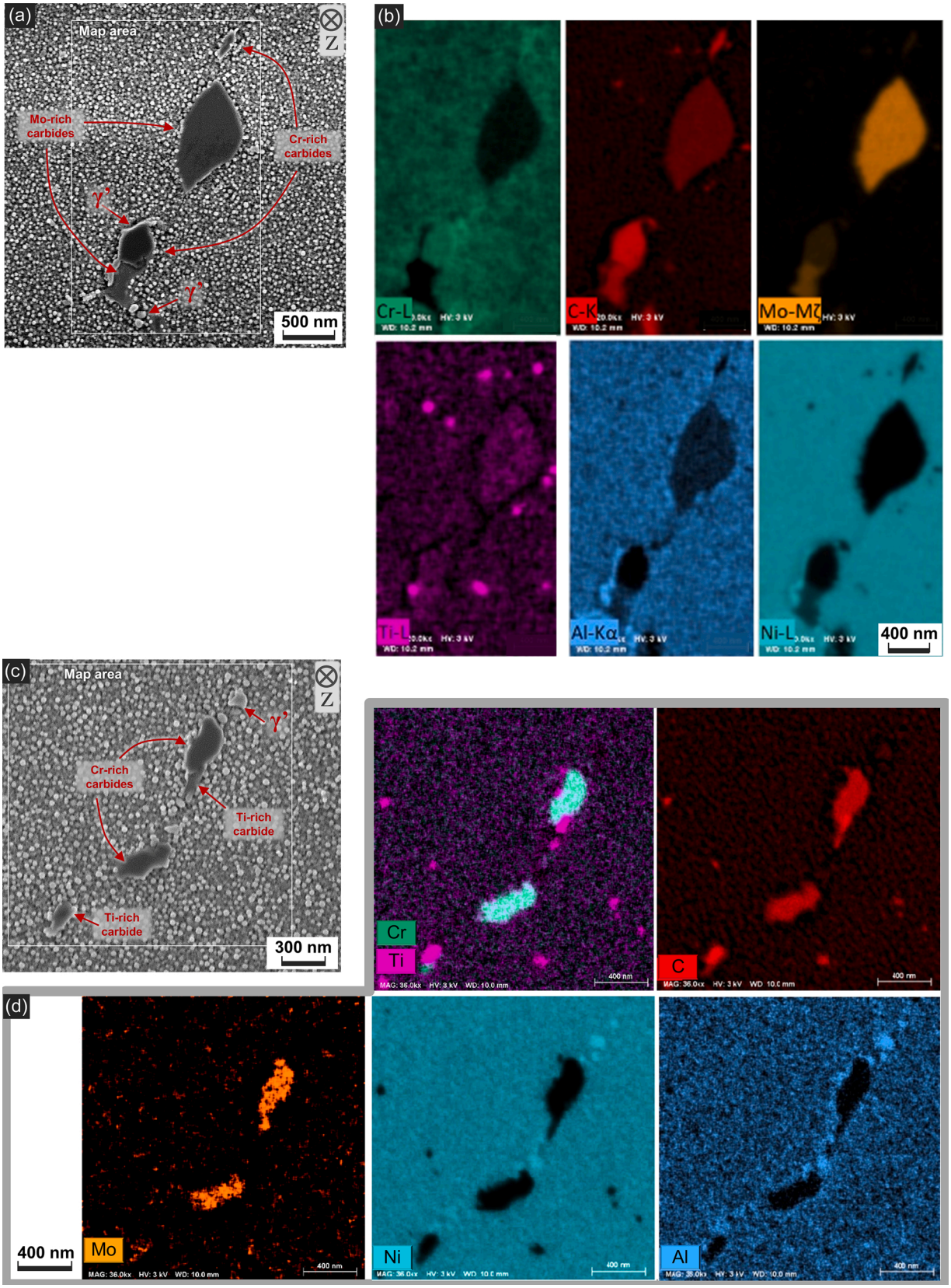

Fig. 7. Microstructure of fully heat-treated LPBF Haynes 282. (a) SE-SEM micrograph of grain boundary region; (b) corresponding EDX maps from (a); (c) SE-SEM micrograph of grain boundary; (d) corresponding EDX maps from (c).

282, it is assumed that the Cr-rich carbides are $M_{23}C_6$-type carbides, which often contain small amounts of Mo. The Mo-rich carbides are likely to be M_6C-type carbides, which have been confirmed in Haynes 282 as occurring separate from $M_{23}C_6$. Ti-rich carbides found inter- and intra-granularly are likely to be MC-type carbides. Although Mo-rich borides are known to occur in Haynes 282, the clear co-indication of C and Mo in the current results excludes the presence of a pure boride phase. Reported borides in Haynes 282 grain boundaries are also significantly smaller in size than the Mo-rich phase seen in Fig. 7 [20,24,34,35].

The measured intra-granular γ' in the heat-treated material was found to be 30 nm ± 9 nm in size, unimodal in distribution, and spherical in morphology. This agrees well with the size and morphology of γ' originally reported for Haynes 282 by Pike [12] and is also comparable to the size reported by other authors (see Table 3) for wrought, cast, and additively manufactured Haynes 282 [23,27–29,34,36,37]. Precipitate size observed in EBM, however, differs significantly owing to ageing and precipitate growth which occurs due to the elevated temperature of the entire built-up material [28].

The mechanical properties were investigated by means of tensile tests at both ambient and elevated temperatures (see Fig. 8). At room temperature the LPBF material in as-built condition showed remarkable ductility, exceeding that of the reference plate material in age-hardened condition. As-built yield strength in the horizontal orientation even exceeded the yield strength of reference age-hardened plate, although significant anisotropy was observed between vertically and horizontally built samples. After the full heat treatment, a significant increase in yield strength and a loss of ductility was observed in the LPBF material. Some decrease in anisotropy was registered as well. While aged LPBF Haynes 282 displays a yield strength more than 200 MPa greater than the reference plate material, the trade-off in ductility means that elongation is lower (but still above 20%) in both build orientations.

At elevated temperature the heat-treated LPBF material retained yield strength matching the reference plate material. Elongation was observed to be lower than that of plate, and an increased anisotropy in elongation was also observed: the vertical samples exhibited double the elongation of the horizontal samples, although this was still below the level of elongation for the reference plate material.

Table 4 shows the results of stress rupture testing and a comparison with reference values from Haynes International. Vertically built samples ruptured after an average of 146.7 hours at the chosen test conditions. This compares favourably to the ~100 hour rupture life for plate material published by Haynes International. Horizontally built samples ruptured much more quickly, after only 45.4 hours on average. However, rupture ductility remained very high for both orientations.

Table 3
Gamma prime size in fully heat-treated LPBF Haynes 282 (current work) and selected references from comparable heat treatment conditions or AM material. DED: directed energy deposition, EBM: electron beam melting.

	Process	Size (nm)	Std dev (nm)
Current work	LPBF	30.0	9.0
Yang et al. 2014 [36]	Cast	42.0	–
Joseph et al. 2017 [23]	Wrought	50.0	–
Zhang et al. 2018 [27]	Wrought	49.8	0.3
Hanning et al. 2019 [34]	Wrought	18.4	3.0
Shin et al. 2019 [37]	Wrought	17.3	3.9
Ramakrishnan et al. 2019 [29]	AM - DED	26.0	–
Unocic et al. 2020 [28]	AM - EBM	100.0	26.0

4. Discussion

4.1. As-built microstructure

The virtually fully dense microstructure shows that Haynes 282 maintained good processability in LPBF and was not subject to hot cracking, which has been reported for some other, higher γ'-fraction superalloys such as IN738LC and CM247LC [5–7,17]. No specialized hardware (such as build plate preheating or powder bed induction heating) was required to successfully process the material. At >99.9%, the density of the LPBF-manufactured Haynes 282 in this study was greater than that of EBM-manufactured material (99.5%) [28] and previous reported LPBF material (~99.7%) [11]. This is an encouraging result for the adoption of Haynes 282 in LPBF, which is currently the most widely industrialized metal AM method [38].

The dendritic solidification microstructure observed is typical of LPBF-produced Ni-base superalloys [2,39]. The segregation of C, Ti, and Mo to the boundary regions of the dendrites agrees well with the partition coefficients determined by Osoba et al. [19]. Despite having significantly slower kinetics and coarser solidification microstructures, as-cast Haynes 282 and DED Haynes 282 have been reported to have similar trends for elemental segregation as observed in this study [29,40]. The coincidence of Ti, Mo, and C suggested that primary dendrites are bounded by primary (Ti, Mo)C particles, which Osoba et al. [19] have theorized are formed by the eutectic type reaction ($L \rightarrow \gamma + MC$). The frequent occurrence of small intra-granular TiC particles, as seen in Fig. 7, also suggests that MC carbides may be formed during the solidification of Haynes 282 and that intra-granular MC carbides seem to remain stable through heat treatment. TiC is generally known to be the most stable carbide phase in Ni-base superalloys after HfC [41].

The absence of any observable γ' in the as-built microstructure corroborates observations by Deshpande et al. [11] and is possibly due to the extremely fast cooling rates of the material during the LPBF process [16]. Additionally, γ' precipitation kinetics in Haynes 282 are known to be rather slow [12]. The suspected presence of oxides in the solidification microstructure and their effect on mechanical properties remain to be confirmed in further work.

4.2. Heat-treated microstructure

Similar to reporting by Christofidou et al. [10] the grain structure after standard heat treatment was not recrystallized, and no significant grain growth was found to have taken place. This fine and highly columnar grain structure represents a significant departure from the known grain structure of the wrought alloy. However, the constituent phases in the microstructure after heat treatment all appear similar to those reported for wrought material, including γ', MC carbides, M_6C carbides, and $M_{23}C_6$ carbides. The primary MC carbides were transformed to other carbides during heat treatment by reactions with the γ matrix, such as the following:

$$(Ti, Mo)C + (Ni, Cr, Al, Ti) \rightarrow Cr_{21}Mo_2C_6 + Ni_3(Ti, Al)$$ and

$$(Ti, Mo)C + (Ni, Co, Al, Ti) \rightarrow Mo_3(Ni, Co)_3C + Ni_3(Ti, Al)$$ [24].

Products of such a reaction can be seen in Figs. 6(c) and 7, whereγ' can be observed at the interface of carbides and the matrix. It was noted that Ti is depleted from the grain boundary γ', which may be due to Ti being bound up in the numerous MC carbides. A possible alternative path to the precipitation of $M_{23}C_6$ carbides may be through decomposition of a carbon-saturated γ matrix by the reaction $\gamma \leftrightarrow M_{23}C_6 + \gamma$ [20].

The arrangement of carbides observed was rather different from that of the wrought material. The "stone wall" structure of continuous grain boundary carbides could not be found in LPBF material. This may be explained by the difference in grain size; wrought Haynes 282 typically has a grain size between ASTM grain size numbers 3 and 5 [14]. LPBF material has significantly finer grains, and hence the carbon would be

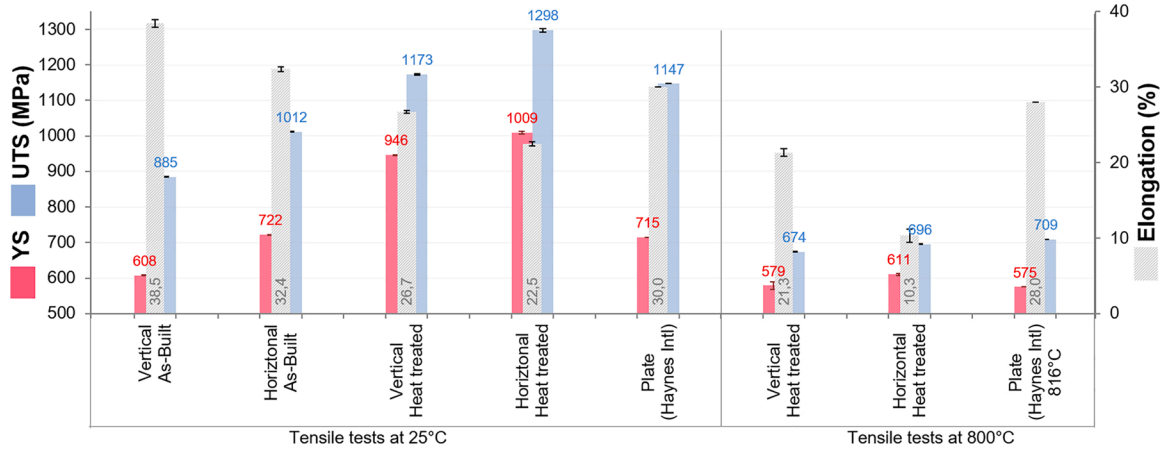

Fig. 8. Tensile properties of LPBF Haynes 282 in as-built and heat-treated conditions at room temperature and 800 °C. Plate data (fully heat-treated) is from Haynes 282 brochure [26] (www.haynesintl.com). YS: yield strength, UTS: ultimate tensile strength.

Table 4
Stress rupture performance of LPBF Haynes 282 at 927 °C and 89 MPa. All tests after standard heat treatment. El: elongation.

Material		Temperature (°C)	Stress (MPa)	Time to Rupture (h)	%El
LPBF	Horizontal	927	89	45.4 ± 1.2	16.7 ± 0.5
LPBF	Vertical	927	89	146.7 ± 15.6	19.3 ± 1.2
Haynes Intl	Plate [26]	927	90	100.0	–

Note: Haynes Intl data from Haynes 282 brochure (www.haynesintl.com). LPBF data is average of 3 samples per condition.

spread over a much larger grain boundary area, resulting in discontinuous grain boundary carbide morphology. While no quantitative analysis of carbides was performed in this work, the same principle may also explain the overall smaller sizes of carbides observed compared to those reported in wrought material [23,24].

The morphology of MC carbides was also a significant departure from what is seen in wrought material. Wrought Haynes 282 contains stringers of large, blocky primary MC carbides and carbo-nitrides which are a residue of the casting and thermomechanical processing steps [23, 42,43]. These hard and brittle particles have been shown to be detrimental to the ductility of the alloy, and they crack during thermomechanical processing. These cracks in the carbides subsequently lead to the initiation of cracks during loading and result in poor tensile ductility [42]. The absence of these carbides from the microstructure of LPBF Haynes 282 may be of some advantage in fatigue performance.

While it is recognized that Haynes 282 has excellent long-term stability at high temperatures [12,36], the fine grain size of the LPBF material may pose a challenge in this regard; as grain boundaries are pathways of high diffusivity, the increased grain boundary area may promote earlier formation of topologically close packed phases. Note that Christofidou et al. performed 1000 hour ageing at 850 °C of LPBF Haynes 282 and did not report any negative effects on microstructure [10]. Finer grain structure, on the other hand, is expected to result in better weldability, as shown by Osoba et al. [20], which may be advantageous for fabrication of large assemblies from AM components. Better understanding of the effect of grain boundary density, and the occurrence of boride phases is an aim of future work.

4.3. Mechanical performance

High yield strength and elongation in the as-built condition, without the presence of strengthening precipitates, is a known property of LPBF-processed material, and is also exhibited by LPBF Haynes 282. The current results seem to indicate that the as-built material shows strength similar to, or exceeding, that of age-hardened plate material, while also retaining an advantage in ductility. Xu et al. explain this exception to the strength-ductility trade-off as being caused by dense networks of dislocations found in the cellular-dendritic structures of the as-built material, resulting in a "pre-work-hardened" state [39]. TEM analysis results by Deshpande et al. also found high dislocation density in as-built LPBF Haynes 282 [11].

Comparison to previously published room temperature mechanical testing results [11] shows that the current results on average have higher yield strength and lower elongation, but with much lower scatter in the values. This is likely due to the higher as-built material density and the lower number of defects.

The observation that the heat-treated LPBF material has a higher yield strength than that of the reference material can conceivably be explained by the grain size hardening effect. Grain boundaries play a key role in strengthening at temperatures below ~$0.5T_m$ (the Hall-Petch effect), and similar properties have been observed for many metal materials fabricated by LPBF [1,41]. This may also explain the anisotropy in yield strength, and the consistently higher yield strengths in the horizontal orientation, where the axis of applied stress coincides with a smaller effective grain size. The lower ductility in the heat-treated condition is in line with the higher strength and is to be expected for a superalloy after precipitation hardening. The small size of the grain boundary carbides, and the lack of carbide stringers, likely resulted in ductile fractures, as can be seen from the fractographs in Fig. 9. In the horizontally oriented room temperature tensile specimens a rather rough fracture surface was observed – as seen in Fig. 9(a) and (b) - characterized by fine dimples mainly located along specific planes, indicating mainly intergranular ductile fracture. Vertically oriented room temperature tensile specimens, which also showed higher ductility, failed by a mixed fracture mode, where higher fraction of transgranular failure with the presence of deep dimples, most probably initiated by carbide particles, as can be seen in Fig. 9(d), was observed in comparison to the horizontally built samples. This is consistent with the higher ductility of the vertically built samples (see Fig. 8). This is also in sharp contrast to the carbide stringers Joseph et al. observed on fracture surfaces which led to reduced ductility in wrought Haynes 282 [42].

Previously reported results for mechanical behaviour of cast and

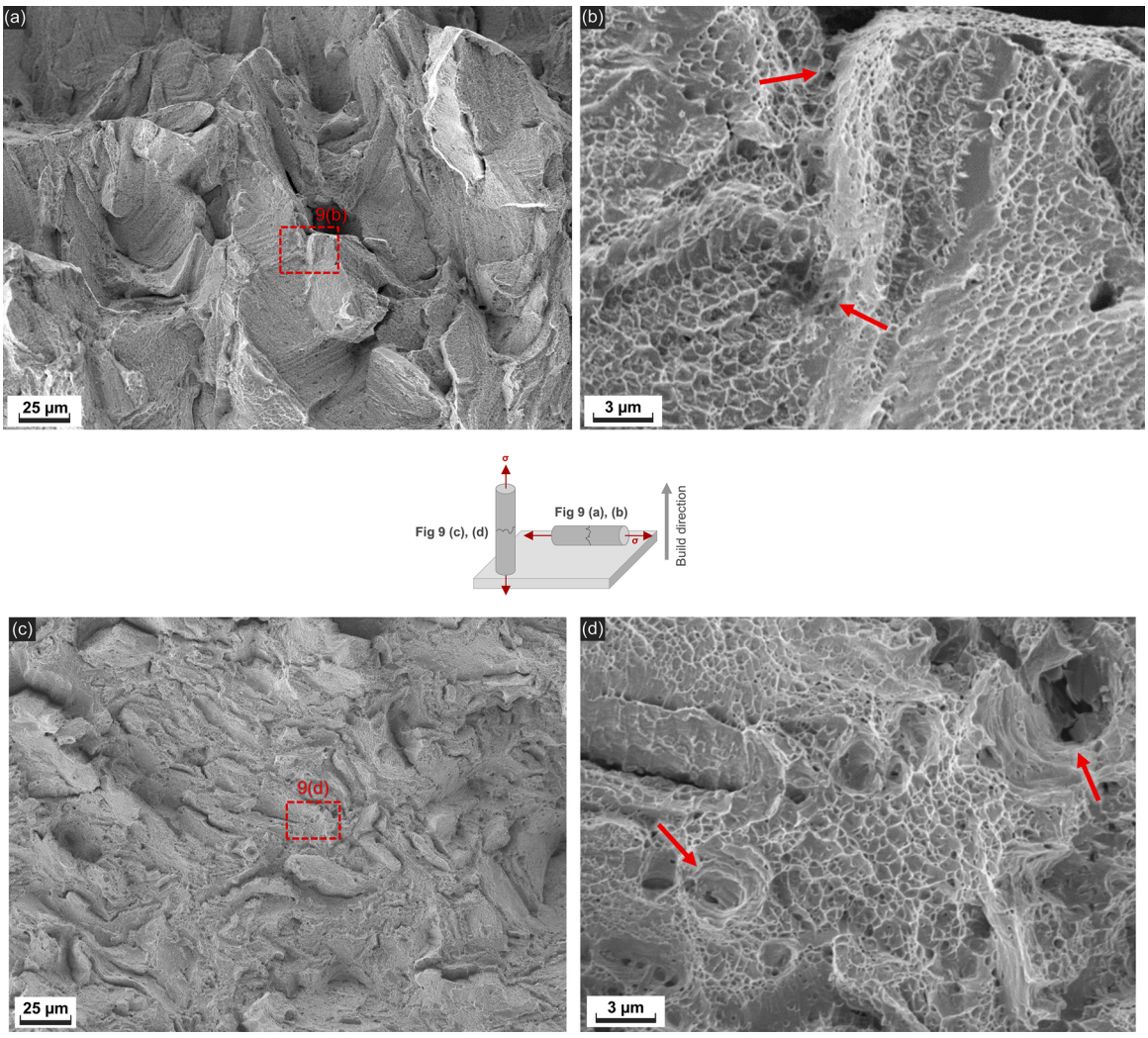

Fig. 9. Fracture surfaces of heat-treated tensile specimens tested at room temperature (a) horizontally built specimen; (b) magnified area showing grain boundaries; (c) vertically built specimen; (d) magnified area showing carbide particles.

wrought Haynes 282 at elevated temperatures showed a decrease in yield strength above 750 °C and a dip in ductility between 750 °C and 850 °C. This decrease in ductility was attributed to the evolution of γ' at this temperature [12,14,34]. Additionally, it is known that deformation mechanisms shift at higher temperatures and larger γ' precipitate sizes, moving from precipitate shearing to Orowan bypassing [27,37]. Furthermore, the increasing influence of creep mechanisms at high testing temperatures may lead to sensitivity of the material to the applied strain rate. Multiple researchers have shown that cooling rates from solution treatment and/or carbide stabilization treatment also have an impact on the γ' size and the ductility at high temperature [37, 44]. In addition to these findings, it is known that grain boundaries contribute less to strengthening at this temperature (above $0.5T_m$) [41].

The high-temperature mechanical properties observed in the current study may be rationalized with several of the above-mentioned mechanisms. The reduced grain boundary strengthening at the testing temperature of 800 °C possibly accounts for the relatively equal yield strengths observed in the horizontal and vertical samples and reference material (note that the plate reference is from tests at 816 °C, whereas LPBF results are at 800 °C). Additionally, grain boundary carbides may act as sites for fracture initiation and subsequent earlier onset of fracture. Horizontally built samples, which have even larger grain boundary area through the axis of applied stress, would therefore demonstrate even lower elongation. Fig. 10 compares representative tensile curves of the room-temperature and high-temperature tensile tests. The figure shows that peak stress is reached at much lower strains at high temperature than at room temperature, suggesting that geometrical instability, leading to necking, occurs much sooner at high temperature. A possible cause for this loss in work hardening ability may be localized stress relaxation during the tensile test. It could also be inferred that, at 800 °C, the reason horizontally built samples fail much sooner than vertically built ones after the start of necking is the faster propagation of cracks. Clear identification of deformation and failure mechanisms of LPBF material at high temperatures, however, is still needed and will be the subject of future studies.

It is well known that microstructures characterized by larger grain sizes are preferred for creep resistance, and that grain boundaries oriented normal to the axis of stress are weak spots in materials during creep deformation [41]. Premature rupture of the horizontally built material (see Table 4) can thus be explained by the larger exposed grain boundary area. As grain boundaries aligned parallel to the axis of stress are not as susceptible to cavitation as those aligned perpendicularly, the vertically oriented samples exceeded the expected rupture life of plate material because their long columnar grain structure is oriented preferentially to the axis of tensile stress. In post-failure analysis (see Fig. 11), many more voids and cracks along grain boundaries were observed in the horizontal sample than in the vertical, confirming that horizontal samples were more susceptible to grain boundary cavitation.

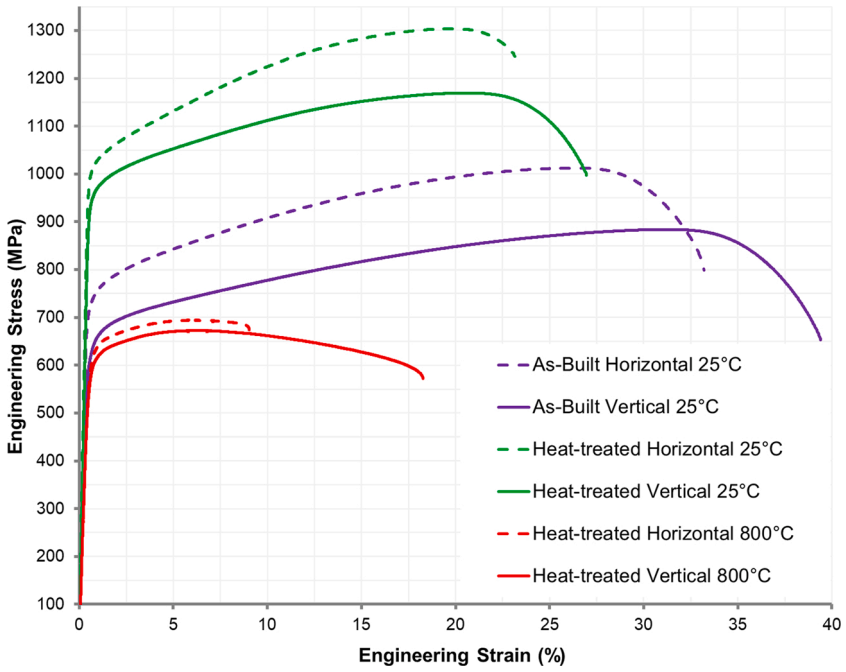

Fig. 10. Representative tensile curves of the room temperature and high-temperature tensile tests.

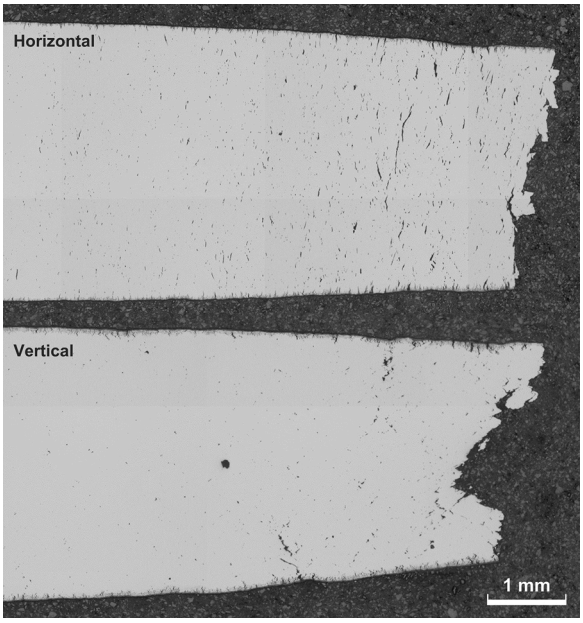

Fig. 11. Cross-sections of vertical and horizontal crept samples.

This significant anisotropy in creep performance has also been reported for other superalloys manufactured using LPBF [17].

While the processability and room-temperature strength of LPBF Haynes 282 have been shown to be favourable, both its fine grain size and anisotropic creep performance might not be desirable characteristics for a high-temperature alloy. This makes the development of tailored heat treatments for LPBF Haynes 282 of special interest. Work by several authors shows that recrystallization and grain growth of fine LPBF grain structures can be brought about by high-temperature heat treatments [17,39,45,46]. Such an approach may be applicable to Haynes 282, given the appreciable window of temperature available between γ' solvus and solidus temperatures of the alloy [10,18,21,47]. Christofidou et al. have demonstrated that heat treatment at 1250 °C for 1 hour can result in full recrystallization of thin samples of LPBF Haynes 282, and Deshpande et al. showed that hot isostatic pressing (HIP) at 1185 °C with 150 MPa pressure can also achieve recrystallized and equiaxed microstructure. Similarly, alternative ageing treatments to enhance carbide and γ' precipitation, as explored by Joseph et al., Polkowska et al., and Christofidou et al. [10,23,24] may prove beneficial and are the subject of further work.

5. Conclusions

The feasibility of additively manufacturing Haynes 282 by LPBF was assessed by evaluating its processability, microstructure, response to heat treatment, and room-temperature and elevated-temperature mechanical properties. The following conclusions can be made based on the results presented in this work:

1 Haynes 282 was manufactured by means of LPBF producing near defect-free material with full density (above 99.98%) and an absence of cracking. The as-built material exhibited a columnar grain structure characteristic for materials produced by LPBF, and finer grain sizes (<30 μm) than are typical for wrought material.
2 The microstructure after heat treatment consisted of γ, γ', and carbide phases similar to those seen in the wrought material. A noteworthy deviation from the wrought material was the morphology of carbides observed for LPBF material, which exhibited fine, discrete grain boundary carbides as opposed to continuous carbide morphology.
3 Room-temperature mechanical properties in the as-built and heat-treated conditions exceeded the properties of the reference material while showing significant anisotropy in terms of build direction. Elevated-temperature mechanical properties at 800 °C displayed comparable yield strength of heat-treated LPBF Haynes 282 to the reference material, however, ductility was significantly reduced. Stress rupture performance was also observed to be highly anisotropic, with the performance of vertically built material exceeding that of the reference material, and horizontally built material displaying shorter rupture life.

4 Further work on detailed microstructure characterisation and strengthening mechanisms as well as tailored post-AM heat treatment is required to reveal the full potential of Haynes 282 by LPBF.

Funding

This work was performed in the framework of the Centre for Additive Manufacturing – Metal (CAM^2), supported by Vinnova.

CRediT authorship contribution statement

Abdul Shaafi Shaikh: Conceptualization, Investigation, Formal analysis, Validation, Writing - original draft, Visualization. **Fiona Schulz:** Validation, Formal analysis, Investigation, Writing - review & editing. **Kevin Minet-Lallemand:** Conceptualization, Methodology, Resources, Supervision, Writing - review & editing, Project administration, Funding acquisition. **Eduard Hryha:** Supervision, Resources, Validation, Writing - review & editing, Project administration, Funding acquisition.

Declaration of Competing Interest

The authors declare that they have no known competing financial interests or personal relationships that could have appeared to influence the work reported in this paper.

Acknowledgements

The authors gratefully acknowledge Professor Johan Ahlström for useful discussions on evaluation of mechanical performance.

References

[1] T. DebRoy, H.L. Wei, J.S. Zuback, T. Mukherjee, J.W. Elmer, J.O. Milewski, A. M. Beese, A. Wilson-Heid, A. De, W. Zhang, Additive manufacturing of metallic components – process, structure and properties, Prog. Mater. Sci. 92 (2018) 112–224, https://doi.org/10.1016/j.pmatsci.2017.10.001.

[2] S.S. Babu, N. Raghavan, J. Raplee, S.J. Foster, C. Frederick, M. Haines, R. Dinwiddie, M.K. Kirka, A. Plotkowski, Y. Lee, R.R. Dehoff, Additive manufacturing of nickel superalloys: opportunities for innovation and challenges related to qualification, Metall. Mater. Trans. A 49 (2018) 3764–3780, https://doi.org/10.1007/s11661-018-4702-4.

[3] V. Navrotsky, A. Graichen, H. Brodin, Industrialisation of 3D printing (additive manufacturing) for gas turbine components repair and manufacturing, VGB PowerTech 12 (2015) 48–52.

[4] N.J. Harrison, I. Todd, K. Mumtaz, Reduction of micro-cracking in nickel superalloys processed by Selective Laser Melting: a fundamental alloy design approach, Acta Mater. 94 (2015) 59–68, https://doi.org/10.1016/j.actamat.2015.04.035.

[5] H. Gruber, Powder Bed Fusion Processing of Ni-base Superalloys: Defect Formation and Its Mitigaton. Doctoral Thesis, Chalmers University of Technology, Gothenburg, Sweden, 2020.

[6] M.M. Attallah, R. Jennings, X. Wang, L.N. Carter, Additive manufacturing of Ni-based superalloys: the outstanding issues, MRS Bull. 41 (2016) 758–764, https://doi.org/10.1557/mrs.2016.211.

[7] O. Adegoke, J. Andersson, H. Brodin, R. Pederson, Review of laser powder bed fusion of gamma-prime-strengthened nickel-based superalloys, Metals 10 (2020) 996, https://doi.org/10.3390/met10080996.

[8] J.H. Boswell, D. Clark, W. Li, M.M. Attallah, Cracking during thermal post-processing of laser powder bed fabricated CM247LC Ni-superalloy, Mater. Des. 174 (2019) 107793, https://doi.org/10.1016/j.matdes.2019.107793.

[9] R. Otto, V. Brøtan, A.S. Azar, O. Åsebø, Processing of Haynes® 282® alloy by laser powder bed fusion technology, in: TMS 2019 148th Annual Meeting & Exhibition Supplemental Proceedings, Springer International Publishing, Cham, 2019, pp. 503–510, https://doi.org/10.1007/978-3-030-05861-6_47.

[10] K.A. Christofidou, H.T. Pang, W. Li, Y. Pardhi, C.N. Jones, N.G. Jones, H.J. Stone, Microstructural control and optimization of Haynes 282 manufactured through laser powder bed fusion, in: S. Tin, M. Hardy, J. Clews, J. Cormier, Q. Feng, J. Marcin, C. O'Brien, A. Suzuki (Eds.), Superalloys 2020, Springer International Publishing, Cham, 2020, pp. 1014–1023, https://doi.org/10.1007/978-3-030-51834-9_99.

[11] A. Deshpande, S. Deb Nath, S. Atre, K. Hsu, Effect of post processing heat treatment routes on microstructure and mechanical property evolution of Haynes 282 Ni-based superalloy fabricated with selective laser melting (SLM), Metals 10 (2020) 629, https://doi.org/10.3390/met10050629.

[12] L.M. Pike, Development of a fabricable gamma prime strengthened superalloy, in: Roger C. Reed, Kenneth A. Green, Pierre Caron, Tim Gabb, Michael G. Fahrmann, Eric S. Huron, Shiela A. Woodard (Eds.), Superalloys 2008 (11th International Symposium), TMS, 2021, pp. 191–200.

[13] M.C. Hardy, M. Detrois, E.T. McDevitt, C. Argyrakis, V. Saraf, P.D. Jablonski, J. A. Hawk, R.C. Buckingham, H.S. Kitaguchi, S. Tin, Solving recent challenges for wrought Ni-Base superalloys, Metall. Mater. Trans. A 51 (2020) 2626–2650, https://doi.org/10.1007/s11661-020-05773-6.

[14] K.L. Kruger, Haynes 282 alloy. Materials for Ultra-Supercritical and Advanced Ultra-Supercritical Power Plants, Elsevier, 2017, pp. 511–545.

[15] H. Gruber, M. Henriksson, E. Hryha, L. Nyborg, Effect of powder recycling in Electron beam melting on the surface chemistry of alloy 718 powder, Metall. Mater. Trans. A 50 (2019) 4410–4422, https://doi.org/10.1007/s11661-019-05333-7.

[16] Y. Li, D. Gu, Parametric analysis of thermal behavior during selective laser melting additive manufacturing of aluminum alloy powder, Mater. Des. 63 (2014) 856–867, https://doi.org/10.1016/j.matdes.2014.07.006.

[17] J. Risse, Additive Manufacturing of Nickel-Base Superalloy IN738LC by Laser Powder Bed Fusion. Doctoral Thesis, RWTH Aachen, Aachen, Germany, 2019.

[18] J. Caron, Weldability and welding metallurgy of Haynes 282 alloy, in: E. Ott, A. Banik, J. Andersson, I. Dempster, T. Gabb, J. Groh, K. Heck, R. Helmink, X. Liu, A. Wusatowska-Sarnek (Eds.), 8th International Symposium on Superalloy 718 and Derivatives, John Wiley & Sons, Inc, Hoboken, NJ, USA, 2014.

[19] L.O. Osoba, R.G. Ding, O.A. Ojo, Microstructural analysis of laser weld fusion zone in Haynes 282 superalloy, Mater. Charact. 65 (2012) 93–99, https://doi.org/10.1016/j.matchar.2011.12.009.

[20] L.O. Osoba, R.G. Ding, O.A. Ojo, Improved resistance to laser weld heat-affected zone microfissuring in a newly developed superalloy HAYNES 282, Metall. Mater. Trans. A 43 (2012) 4281–4295, https://doi.org/10.1007/s11661-012-1212-7.

[21] L.O. Osoba, O.A. Ojo, Influence of laser welding heat input on HAZ cracking in newly developed Haynes 282 superalloy, Mater. Sci. Technol. 28 (2012) 431–436, https://doi.org/10.1179/1743284711Y.0000000078.

[22] D.A. Metzler, A gleeble based method for ranking the Strain Age Cracking susceptibility of Ni-based Superalloys, Weld. J. 87 (2008) 249s–256s.

[23] C. Joseph, C. Persson, M. Hörnqvist Colliander, Influence of heat treatment on the microstructure and tensile properties of Ni-base superalloy Haynes 282, Mater. Sci. Eng. A 679 (2017) 520–530, https://doi.org/10.1016/j.msea.2016.10.048.

[24] A. Polkowska, W. Polkowski, M. Warmuzek, N. Cieśla, G. Włoch, D. Zasada, R. M. Purgert, Microstructure and hardness evolution in Haynes 282 nickel-based superalloy during multi-variant aging heat treatment, J. Mater. Eng. Perform. 28 (2019) 3844–3851, https://doi.org/10.1007/s11665-019-3886-0.

[25] K.A. Unocic, D. Shin, X. Sang, E. Cakmak, P.F. Tortorelli, Single-step aging treatment for a precipitation-strengthened Ni-based alloy and its influence on high-temperature mechanical behavior, Scr. Mater. 162 (2019) 416–420, https://doi.org/10.1016/j.scriptamat.2018.11.045.

[26] HAYNES® 282® alloy: Material Brochure, Haynes International, 2019. http://haynesintl.com/docs/default-source/pdfs/new-alloy-brochures/high-temperature-alloys/brochures/282-brochure.pdf?sfvrsn=20.

[27] P. Zhang, Y. Yuan, H. Yin, Y. Gu, J. Wang, M. Yang, G. Yang, X. Song, Tensile properties and deformation mechanisms of Haynes 282 at various temperatures, Metall. Mater. Trans. A 49 (2018) 1571–1578, https://doi.org/10.1007/s11661-018-4515-5.

[28] K.A. Unocic, M.M. Kirka, E. Cakmak, D. Greeley, A.O. Okello, S. Dryepondt, Evaluation of additive electron beam melting of Haynes 282 alloy, Mater. Sci. Eng. A (2019) 138607, https://doi.org/10.1016/j.msea.2019.138607.

[29] A. Ramakrishnan, G.P. Dinda, Microstructure and mechanical properties of direct laser metal deposited Haynes 282 superalloy, Mater. Sci. Eng. A 748 (2019) 347–356, https://doi.org/10.1016/j.msea.2019.01.101.

[30] A. Leicht, M. Rashidi, U. Klement, E. Hryha, Effect of process parameters on the microstructure, tensile strength and productivity of 316L parts produced by laser powder bed fusion, Mater. Charact. 159 (2020) 110016, https://doi.org/10.1016/j.matchar.2019.110016.

[31] M.-S. Pham, B. Dovgyy, P.A. Hooper, C.M. Gourlay, A. Piglione, The role of side-branching in microstructure development in laser powder-bed fusion, Nat. Commun. 11 (2020) 749, https://doi.org/10.1038/s41467-020-14453-3.

[32] V.D. Divya, R. Muñoz-Moreno, O.M.D.M. Messé, J.S. Barnard, S. Baker, T. Illston, H.J. Stone, Microstructure of selective laser melted CM247LC nickel-based superalloy and its evolution through heat treatment, Mater. Charact. 114 (2016) 62–74, https://doi.org/10.1016/j.matchar.2016.02.004.

[33] D. Deng, R.L. Peng, H. Brodin, J. Moverare, Microstructure and mechanical properties of Inconel 718 produced by selective laser melting: sample orientation dependence and effects of post heat treatments, Mater. Sci. Eng. A 713 (2018) 294–306, https://doi.org/10.1016/j.msea.2017.12.043.

[34] F. Hanning, A.K. Khan, J. Steffenburg-Nordenström, O. Ojo, J. Andersson, Investigation of the effect of short exposure in the temperature range of 750–950 °C on the ductility of Haynes® 282® by advanced microstructural characterization, Metals 9 (2019) 1357, https://doi.org/10.3390/met9121357.

[35] L.O. Osoba, A.K. Khan, O.A. Ojo, Identification of Mo-based precipitates in Haynes 282 superalloy, Metall. Mater. Trans. A 48 (2017) 1540–1543, https://doi.org/10.1007/s11661-017-3999-8.

[36] Y. Yang, Microstructural evolution in cast Haynes 282 for application in advanced powerplants, in: D. Gandy, J. Shingledecker (Eds.), Advances in Materials Technology for Fossil Power Plants: Proceedings from the Seventh International Conference (EPRI 2013), ASM International, Waikoloa, Hawai, 2013, pp. 143–154.

[37] K.-Y. Shin, J.-H. Kim, M. Terner, B.-O. Kong, H.-U. Hong, Effects of heat treatment on the microstructure evolution and the high-temperature tensile properties of

Haynes 282 superalloy, Mater. Sci. Eng. A 751 (2019) 311–322, https://doi.org/10.1016/j.msea.2019.02.054.
[38] W. Associates, Wohlers Report 2020: 3D Printing and Additive Manufacturing Global State of the Industry, Wohlers Associates, Fort Collins (Colo.), 2020.
[39] J. Xu, H. Gruber, R. Boyd, S. Jiang, R.L. Peng, J.J. Moverare, On the strengthening and embrittlement mechanisms of an additively manufactured Nickel-base superalloy, Materialia 10 (2020) 100657, https://doi.org/10.1016/j.mtla.2020.100657.
[40] N. Sobczak, Z. Pirowski, R.M. Purgert, W. Uhl, K. Jaskowiec, L. Boron, S. Pysz, J. J. Sobczak, Castability of Haynes 282 alloy. Advanced Ultrasupercritical Coal-Fired Power Plants, 2012.
[41] C.T. Sims, N.S. Stoloff, W.C. Hagel, Superalloys II: High-Temperature Materials for Aerospace and Industrial Power, Wiley, 1987.
[42] C. Joseph, M. Hörnqvist, C. Persson, Anisotropy of room temperature ductility in Haynes 282 forgings, in: E. Ott, A. Banik, J. Andersson, I. Dempster, T. Gabb, J. Groh, K. Heck, R. Helmink, X. Liu, A. Wusatowska-Sarnek (Eds.), 8th International Symposium on Superalloy 718 and Derivatives, John Wiley & Sons, Inc, Hoboken, NJ, USA, 2014.
[43] C.J. Boehlert, S.C. Longanbach, A comparison of the microstructure and creep behavior of cold rolled HAYNES® 230 alloy™ and HAYNES® 282 alloy™, Mater. Sci. Eng. A 528 (2011) 4888–4898, https://doi.org/10.1016/j.msea.2011.03.019.
[44] C. Joseph, Microstructure Evolution and Mechanical Properties of Haynes 282. Doctoral Thesis, Chalmers University of Technology, Gothenburg, Sweden, 2018.
[45] J. Xu, H. Gruber, D. Deng, R.L. Peng, J.J. Moverare, Short-term creep behavior of an additive manufactured non-weldable Nickel-base superalloy evaluated by slow strain rate testing, Acta Mater. 179 (2019) 142–157, https://doi.org/10.1016/j.actamat.2019.08.034.
[46] S. Banoth, C.-W. Li, Y. Hiratsuka, K. Kakehi, The effect of recrystallization on creep properties of alloy IN939 fabricated by selective laser melting process, Metals 10 (2020) 1016, https://doi.org/10.3390/met10081016.
[47] H. Matysiak, M. Zagorska, J. Andersson, A. Balkowiec, R. Cygan, M. Rasinski, M. Pisarek, M. Andrzejczuk, K. Kubiak, K.J. Kurzydlowski, Microstructure of Haynes® 282® superalloy after vacuum induction melting and investment casting of thin-walled components, Materials (Basel, Switzerland) 6 (2013) 5016–5037, https://doi.org/10.3390/ma6115016.